Single and Multi-Mode Directional Lasing from Arrays of Dielectric Nanoresonators

*Shaimaa I. Azzam, Krishnakali Chaudhuri, Alexei Lagutchev, Zubin Jacob, Young L. Kim, Vladimir M. Shalaev, Alexandra Boltasseva, and Alexander V. Kildishev**

We dedicate this paper to Prof. Mark I. Stockman, our teacher, colleague, and friend

The strong electric and magnetic resonances in dielectric subwavelength structures have enabled unique opportunities for efficient manipulation of light–matter interactions. Besides, the dramatic enhancement of nonlinear light–matter interactions near so-called bound states in the continuum (BICs) has recently attracted enormous attention due to potential advancements. However, the experimental realizations and the applications of high-Q factor resonances in dielectric resonances in the visible have thus far been considerably limited. In this work, the interplay of electric and magnetic dipoles in arrays of dielectric nanoresonators is explored. The experimental realization of high-Q factor resonances in the visible through the collective diffractive coupling of electric and magnetic dipoles is reported. It is also shown that coupling the Rayleigh anomaly of the array with the dipoles of the individual nanoresonators can result in the formation of different types of BICs. The resonances in the visible regime is utilized to achieve lasing action at room temperature with high spatial directionality and low threshold. Finally, multi-mode, directional lasing is experimentally demonstrated and the BIC-assisted lasing mode engineering in arrays of dielectric nanoresonators is studied. It is believed that the results enable a new range of applications in flat photonics through realizing on-chip controllable single and multi-wavelength micro-lasers.

1. Introduction

Bound states in the continuum (BICs) are dark states that stay localized even though they coexist with the structure's radiation continuum.[1–8] Ideal BICs have infinite lifetime and require at least one dimension of the structure to extend to infinity.[6] In practical realizations, due to perturbations and finite extent, the BIC collapses to a Fano resonance with a limited (yet still very long) lifetime—a regime known as quasi-BIC.[6,9] Besides, in the vicinity of the BIC, near-BIC high-Q resonances can be attained by slightly detuning the system from the BIC point.[10–12] Near-BIC resonances are generally stable to fabrication imperfections as they can be obtained at a relatively broad interval of a system parameter values compared to BICs, which are typically achieved at a single point.[11,12] Photonic structures supporting BICs have been intensively studied over the last decade as they offer unique ways for engineering and enhancing the light–matter interactions.[6–8,10,13–16] Photonic BICs have to date enabled a plethora of applications, including light routing,[17] nonlinear enhancement,[18] sensing,[19] and lasing.[20–23] BIC-based lasers are of special interest due to their unique advantages such as miniaturized footprint with all-dielectric materials which makes them suitable for on-chip lasers.[24,25] However, the experimental realizations of BICs and their applications in the visible wavelength range have been considerably limited and started to gain interest only recently.[22,24,26]

The emergence of dielectric nanoresonators with strong electric and magnetic responses has enabled fundamentally new ways of engineering light–matter interactions.[27,28] The interplay between electric and magnetic resonances in a dielectric nanoresonator enables control over the direction of scattering, along with the spectral position, strength, and quality factor of the resonance.[29] This control can be realized in a single scatterer by tuning its shape to support a desired electromagnetic response[30] Additionally, arranging the nanoresonators in a lattice can influence their spectral response providing more

Dr. S. I. Azzam, Dr. K. Chaudhuri, Dr. A. Lagutchev, Prof. Z. Jacob, Prof. V. M. Shalaev, Prof. A. Boltasseva, Prof. A. V. Kildishev
School of Electrical & Computer Engineering and Birck Nanotechnology Center
Purdue University
West Lafayette, IN 47907, USA
E-mail: kildishev@purdue.edu

Dr. S. I. Azzam, Dr. K. Chaudhuri, Dr. A. Lagutchev, Prof. Z. Jacob, Prof. V. M. Shalaev, Prof. A. Boltasseva, Prof. A. V. Kildishev
Purdue Quantum Science and Engineering Institute
Purdue University
West Lafayette, IN 47907, USA

Prof. Y. L. Kim
Weldon School of Biomedical Engineering
Purdue University
West Lafayette, IN 47907, USA

The ORCID identification number(s) for the author(s) of this article can be found under https://doi.org/10.1002/lpor.202000411

DOI: 10.1002/lpor.202000411

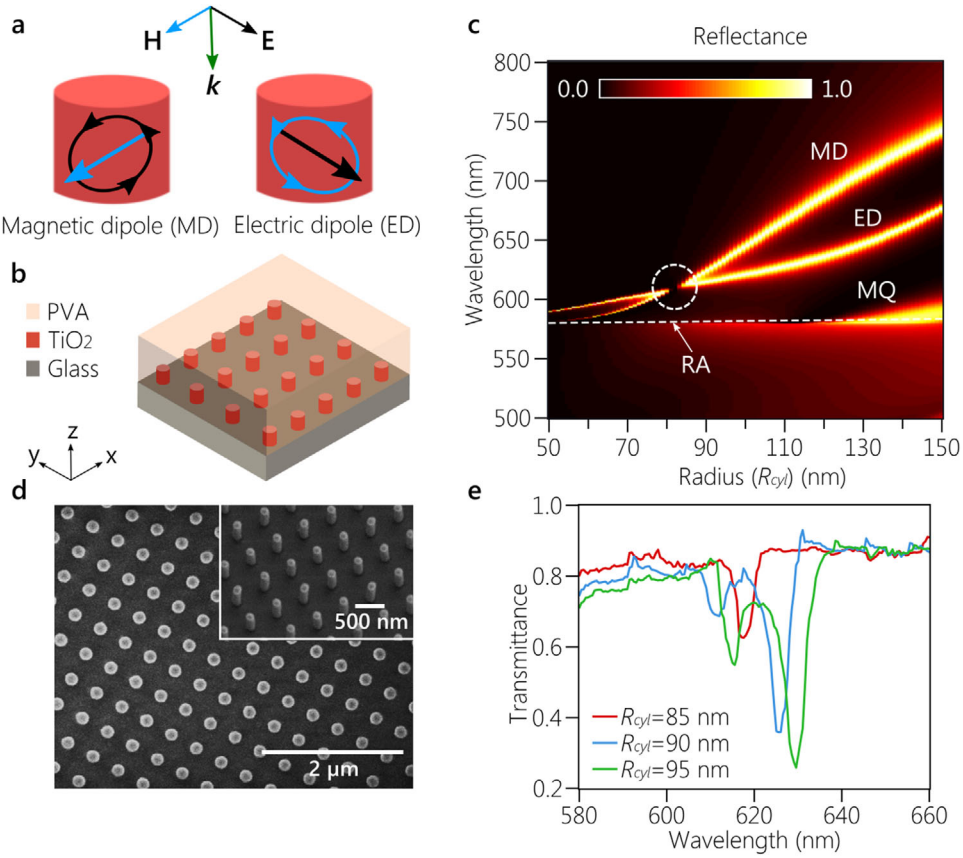

Figure 1. High-Q resonances in arrays of dielectric nanoresonators with electric and magnetic dipoles. a) Electric and magnetic dipole resonances supported by a dielectric nanoresonator. b) A schematic of the array structure with a square lattice of 400 nm period made of titanium oxide (TiO_2) cylindrical nanoresonators with a height of 300 nm on a glass substrate and covered with polyvinyl alcohol (PVA). c) Simulated reflectance as a function of the nanoresonator radius (R_{cyl}). The dashed white circle shows the disappearance of the resonance, indicating the realization of the Kerker condition at $R_{cyl} = 82$ nm and $\lambda = 610$ nm. The three resonances correspond to the magnetic dipole (MD), electric dipole (ED), and the magnetic quadrupole (MQ), respectively and the dashed white line shows the Rayleigh anomaly (RA) of the array. d) An scanning electron microscope image of the fabricated structure. e) The measured transmittance of the array with radii of 85, 90, and 95 nm.

degrees of control over light–matter interaction.[31–33] Coupling between the electric dipole (ED) and magnetic dipole (MD) in individual dielectric resonators can be controlled by placing the resonators in close proximity to engage their near field interaction. However, due to the high refractive index of dielectric nanoresonators' materials, the electromagnetic field is generally tightly confined inside the resonator and near field coupling is relatively low. Collective diffractive coupling of EDs and MDs has been proposed as a more effective way of controlling the response of dielectric nanoresonators arrays.[32,33] This can be achieved through the coupling of ED and MD resonances in an array of dielectric scatterers to the Rayleigh anomaly (RA) of the array.

In this work, we investigate the experimental realization of high-Q factor coupled ED and MD resonances supported in the visible range by the array of dielectric nanoresonators due to their collective interaction. Furthermore, we demonstrate lasing action within the visible spectrum, relying on the high-Q resonances supported by arrays of nanoresonators. The laser operates at room temperature with high beam directionality and low-threshold. In addition, we experimentally investigate the BIC-assisted mode engineering in arrays of dielectric nanoresonators, and we show multi-wavelength directional lasing. Two- and three-mode lasers have been demonstrated experimentally, showing the potential for this type of structure to support controllable multi-wavelength on-chip microlasers. It is important to mention that other reports of room-temperature lasing action in the visible have been recently demonstrated using a similar nanostructures array.[26]

2. Results

A dielectric resonator can generally support both electric and magnetic dipole resonances. **Figure 1**a shows an illustration of in-plane MD and ED resonances. Out-of-plane resonances can also be excited in the dielectric resonators as dipoles with vertical orientations. Here, we study an array comprising TiO_2 cylindrical nanoresonators with a height of 300 nm arranged in a square lattice with a period of 400 nm on a silica glass substrate, Figure 1b. The structure is covered with a polymer that index-matched to the substrate. Our choice of materials and dimensions are to achieve resonances in the visible wavelength range.

Figure 1c shows the reflectance spectra of the array as a function of the radius of the nanoresonators. Three resonances corresponding to the ED, MD as well as a magnetic quadrupole (MQ) can be observed in the reflectance spectra, as indicated in Figure 1c. The resonance classification is accomplished based on the displacement current loops and E-field profiles; more information can be found in Section S1, Supporting Information. The RA of the array is depicted as a dashed white line in Figure 1c. As the radius of the nanoresonators decreases, the linewidth of the MD resonance gets narrower and the position of the MD approaches that of the RA. Both observations are distinctive features of the diffractive coupling.[32] We also notice that the spectral position of the MQ follows the RA closely. The ED and MD modes spectrally overlap a radius of 82 nm, and a wavelength of 610 nm, highlighted by the dashed circle in Figure 1c confirming the realization of Kerker's condition. Almost zero light reflection is realized at the Kerker point with a near-unity unidirectional transmission. Another feature that results from the diffractive coupling of the dipoles to the RA is the enhancement of electromagnetic fields (Figure S2, Supporting Information) which is very advantageous in boosting the nonlinear phenomenon. More insight can also be gained from studying the effect of the nanoresonator height on the spectral positions and widths of the ED, MD, and MQ in Section S2, Supporting Information.

A scanning electron microscope image of the fabricated structure is given in Figure 1d. For details of the fabrication, see the Experimental Section and Figure S5, Supporting Information. Transmittance at normal incidence from a few samples with different R_{cyl} was characterized using spectroscopic ellipsometry, Figure 1e. A single resonance is observed at a radius value of 85 nm where the ED and MD start to overlap, as can be noticed from Figure 1e. At larger radii values, 90 and 95 nm, two dips corresponding to the ED and MD are observed. The measured transmittance is in very good agreement with the simulated spectra, Figure S4, Supporting Information. However, due to the non-uniformity in the radii of the fabricated sample, the measured resonances are broadened, and their dip positions are slightly shifted compared to the simulated ones with around 5 nm.

2.1. Mode Engineering and BIC States in Arrays of Dielectric Nanoresonators

By engineering the geometrical and material parameters of a unit-cell dielectric resonator, we can selectively excite distinct resonant modes and also tune their spectral properties.[34,35] Therefore, an optimal unit-cell design can enable excellent control over the band-diagram of the entire structure array. In general, band-diagram engineering can be accomplished through geometrical optimization which when applied to metasurfaces, results in complex shapes with astringent unit cell geometries and dimensions leading to further fabrication constraints.[34–36] To perform mode engineering in our study, we intentionally limit the structure design to a simple, easy-to-fabricate square array of TiO_2 cylinders. A unit-cell of this type appears to be an ideal prototype for analyzing the interplay between the electric and magnetic responses in a dielectric nanoresonator, studying the array effect, as well as exploiting the intriguing physics of BICs.

Figure 2 shows the simulated reflectance of two arrays under transverse electric (TE) and transverse magnetic (TM) polarizations. Each of these arrays comprising nanoresonators each with a different radius throughout the whole array. Figure 2a shows the reflectance of an array with radius $R_{cyl} = 80$ nm illuminated with TE polarization as a function of the angle of incidence and wavelength. The resonance at the Γ point around 612 nm corresponds to a BIC due to an out-of-plane MD, which is later used as feedback for the single-mode lasing. Another BIC appears at the Γ point around 589 nm that is due to a magnetic quadrupole (MQ). Both these BICs are symmetry-protected and are highlighted in the inset of **Figure 2**a. Figure 2c shows the reflectance of the same array, $R_{cyl} = 80$ nm, with TM-polarized light. The resonance at the Γ point around 610 nm corresponds to the point where the in-plane ED and the MD start to overlap, as shown in Figure 1c. In the TM reflectance, the array supports two types of BIC states, one at the Γ point with wavelength 669.2 nm, which is a symmetry-protected state. Additionally, an off-Γ Friedrich–Wintgen (FW) BIC is also supported at 8∘ at a wavelength of 741 nm.[5,6] The FW BIC is highlighted with a dotted white circle in Figure 2a and magnified in the inset. This emphasizes the ability of an array with such a simple unit cell structure to support multiple types of resonances with different underlying physics. Not only can this structure support a simple "band-edge" mode at the Γ point, but it also provides access to the non-trivial FW BIC states that are not symmetry-protected and hence are more resilient to structural imperfections.

The structure with $R_{cyl} = 100$ nm shows a different reflectance response as seen in Figure 2c,d. Under the TE illumination, 2c two symmetry-protected BICs at around 655 and 606 nm are observed similar to the previous structure. Besides, at the Γ point, we observe two additional resonances due to the in-plane MD and ED at 646 and 622 nm, respectively. Moreover, with the TM polarization, the array with $R_{cyl} = 100$ nm supports a symmetry-protected BIC at 683 nm, as well as an FW BIC at 824 nm and 11.5° as can be seen in 2d. The stark difference between the optical response of the two designs suggests an excellent opportunity to engineer the band-edge and bandgap of metasurfaces by tuning their geometrical parameters. In the next section, we investigate the application of such arrays of dielectric nanoresonators in single and multi-wavelength lasing.

2.2. Lasing in Arrays of Dielectric Nanoresonators

After the successful demonstration of the passive nanoresonator arrays with relatively high-Q factor resonances, we employ such resonances to provide feedback for lasing action in the visible spectrum. First, the index matching coating is washed off. Then, the array is spin-coated with polyvinyl alcohol (PVA) solution of an organic gain medium (Rhodamine 101) with a concentration of 10 mM, which acts as an active material. The spin coating yields an active layer with a thickness of ≈2 μm. For the single wavelength laser, we use an array with $R_{cyl} = 80$ nm, which has a BIC at 612 nm due to the out-of-plane MD. To characterize the lasing action, the sample is pumped with the second-harmonic output from an Nd: YAG laser (532 nm, 1-Hz repetition rate, and 400-ps pulse duration). The emitted light is collected through fiber and directed to a spectrometer to get the emission spectrum to

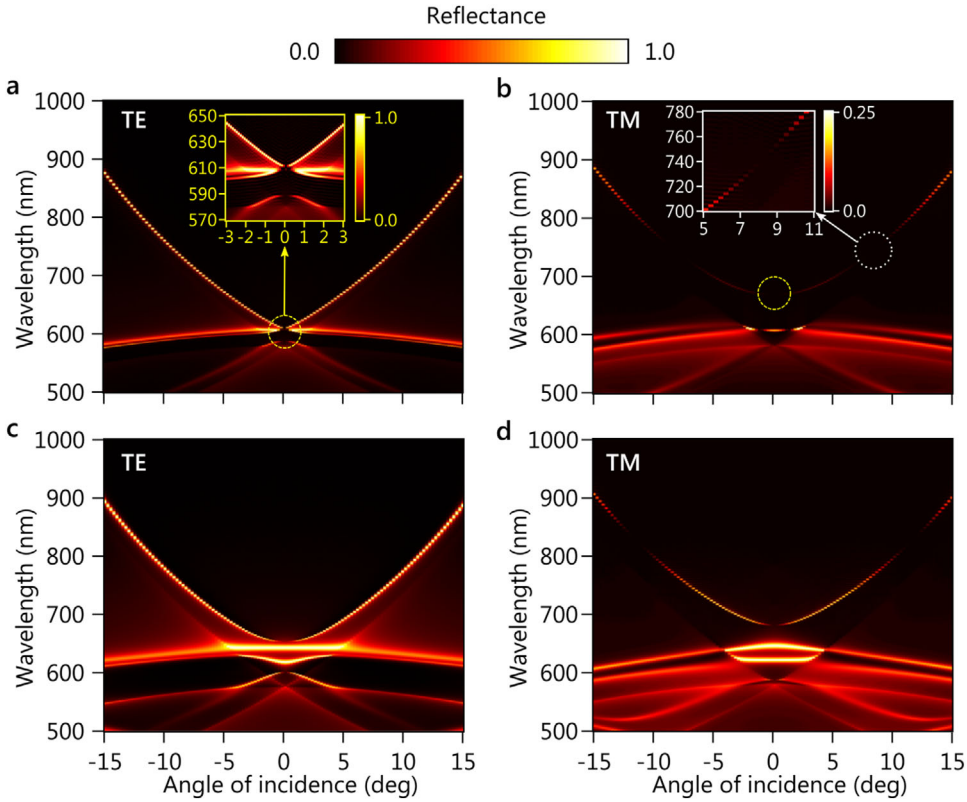

Figure 2. The simulated reflectance versus the angle of incidence and wavelength. The reflectance of an array with TiO_2 cylinder nanoresonators (R_{cyl} = 80 nm) using a) TE-polarized light, and b) TM-polarized light. The dashed yellow circle at the Γ point in (a) highlights the two symmetry-protected BICs at 589nm and 612 nm, which are magnified in the inset. The dotted white circle in (b) highlights the off-Γ (Friedrich-Wintgen, FW) BIC, which is zoomed in in the inset at 741 nm. The reflectance from an array with R_{cyl} = 100 nm with c) TE-polarized light, and d) TM-polarized light. Under TE polarization (c), two symmetry-protected BICs are observed at 606 nm and 655 nm and with TM polarization (d), the array supports a symmetry-protected BIC at the Γ point and 683 nm and an FW BIC at 824 nm and 11.5°.

demonstrate the two critical effects of lasing; threshold and spectral narrowing. The setup schematic is given in Figure S7, Supporting Information and details of the experiment can be found in the Experimental Section.

Figure 3a depicts the evolution of the collected emission spectra as the pump fluence increases showing a narrow lasing peak emerging around 614 nm. An apparent threshold behavior is observed where the emission transitions from enhanced spontaneous to stimulated emission at around 40 μJ cm^{-2}, as evident from the experimental (Figure 3b) and simulated (Figure 3c) data. This process is accompanied by a significant narrowing of the emission spectral width from >30 nm to <1 nm, as observed in the experiment (Figure 3d), and numerical simulations (Figure 3e). The emission directionality is characterized using back focal plane measurements, see the Experimental Section. Below the lasing threshold, the enhanced spontaneous emission is illustrated with a back focal plane cross-section and the emission pattern of Figure 3f with the cross-section showing a relatively wide spatial spread. However, above the threshold, the same measurements (see Figure 3g) indicate tightly focused spots and narrow beams at 3.5° with a less than 0.8° in beamwidth. It is worth mentioning that due to our structure's square lattice, the back focal plane image should consist of two points along the *x*-axis and two along the *y*-axis. However, Figure 3f shows only a pair of bright spots along the *x*-axis, which is a result of the polarization of the pump. When an analyzer with orthogonal orientation (along the *y*-axis) is introduced in the lasing emission path before collection, we observe four bright spots in the back focal plane emission as expected, Figure S8, Supporting Information. All our experimental studies are guided and supported by the advanced multiphysics numerical framework built on coupling carrier kinetics with a full-wave time-domain Maxwell equation solver.[37] Details of the numerical simulations can be found in the Experimental Section and Section S2, Supporting Information.

On-chip multi-mode lasers are invaluable tools for many applications such as optical signal processing, quantum computing, wavelength multiplexing for telecommunication, and others. Here, we explore the engineering of the various resonance in play in our structure to realize multi-mode lasing. We design, fabricate, and experimentally demonstrate dual- and triple-mode laser solely based on the optimal choice of the radius of the dielectric resonators in the BIC-type metasurface array. As mentioned earlier, due to the choice of the geometrical parameters of the resonators and their arrangement in a lattice, multiple BICs can be supported at the Γ-point due to the suppressed radiation from the vertical dipoles (ED and MD) as well as the quadruple. Due to the carrier diffusion and the inhomogeneous broadening in the gain material, multiple modes can start to lase if there

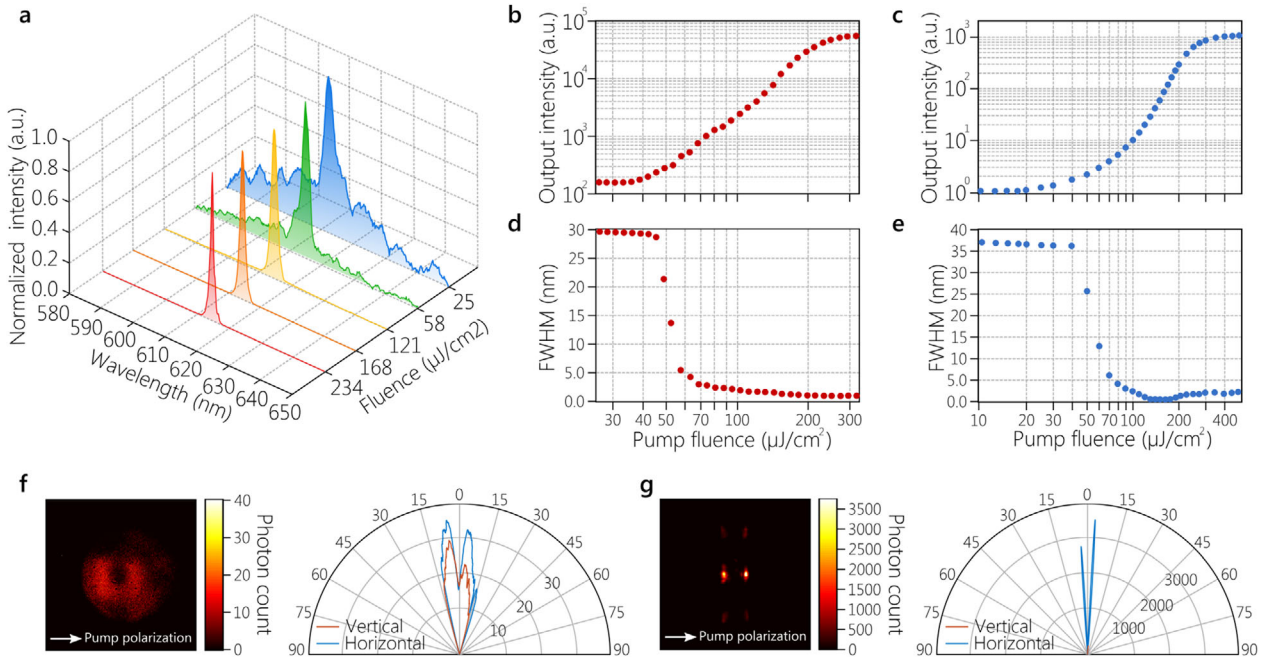

Figure 3. Lasing action with near-BIC feedback. a) The evolution of the emission spectra collected from the gain-coated structure with the increased pump fluence, showing a transition from amplified spontaneous emission to lasing. b,c) The experimental (b) and simulated (c) output intensities versus the pump fluence. d,e) The experimental (d) full width at half-maximum (FWHM) and simulated (e) FWHM as a function of pump fluence. f,g) Back focal plane image and the radiation patterns, which are vertical and horizontal cross-sections of the focal plane image, of the laser emission below (f) and above (g) lasing threshold. White arrows in f, g show the polarization of the pump laser.

is sufficient spectral overlap with the spectral width of the gain medium. **Figure 4** shows the lasing dynamics from an array with nanoresonators with $R_{cyl} = 95$ nm and a ≈2 μm active cover layer of Rhodamine 101 in PVA. The reflectance spectrum of this array is very similar to the one shown in Figure 2c,d. Under the TE-polarized light, the array with $R_{cyl} = 95$ nm supports two BICs at the Γ-point; one at 635 nm due to an out-of-plane magnetic dipole and the other at 600 nm originated from the MQ. With increased pump intensity, one laser peak emerges at a threshold of ≈60 μJ cm^{-2} around 610 nm. At a pump fluence of 140 μJ cm^{-2}, another peak appears at 617.5 nm, as seen in Figure 4a. The evolution of the intensity of both laser peaks versus the pump fluence can be seen in Figure 4b. A rotating analyzer is used before feeding the collected emission to the spectrometer to study the polarization properties of the laser emission. Back-focal plane images of the laser emission at different analyzer angles are depicted in Figure 4c. At 0° analyzer angle, Figure 4c (left) shows that laser emission takes the shape of two spatial beams. However, an analyzer angle of 90°, Figure 4c (right) shows the appearance of two additional beams. The change of the measured peak values of both lasing wavelengths, 610 and 617 nm, is plotted in Figure 4d. We can note that the laser peak at 617.5 nm shows little sensitivity to the analyzer rotation, dropping to only half of its maximum value at the analyzer angle of 90°. However, the peak at 610 nm is much more sensitive to the analyzer orientation. At an analyzer angle of 90°, the peak intensity of the 610 nm beam drops to ≈10% of its maximum value (at 0° angle). From Figure 4d, we can see that when the analyzer angle is set to 90°, the peak amplitude of the two laser wavelengths is almost equal. From this, we conclude that each wavelength emits in a different spatial direction. The beam at 610 nm emits at 4.6° with a beamwidth of 2°, and the laser peak at 617.5 nm has a spatial beam around 7.9° with a 1.6° beamwidth as calculated from the back-focal plane image in Figure 4c (right). Triple-mode lasing has also been observed and reported in Figure S9, Supporting Information.

It is worth mentioning that our choice for the unit cell for the multi-mode operation is a proof-of-concept and is simply based on the number of supported resonances. Further optimized unit cells can be investigated to provide equal peak amplitude, controllable threshold, and spectral separation. Achieving multi-mode on-chip lasing will open up a multitude of opportunities in optical computing, sensing, and telecommunications. Our design and methodology represent a step on the way to realize low threshold room-temperature nanolasers with multiple wavelengths and high directionality. Future directions will include optimization mechanisms that take full advantage of the interplay between the electric and magnetic responses in dielectric resonators alongside the rich physics of BICs to gain control of the characteristics of each lasing peak as well as their spectral separation.

3. Conclusion

In summary, we design, fabricate, and experimentally demonstrate high-Q factor resonances in arrays of dielectric nanoresonators in the visible wavelength range. We utilize the proposed all-dielectric arrays to experimentally demonstrate highly-directional, low-threshold lasing action in an organic dye coating layer. Our experimental studies are guided and supported by the advanced multiphysics numerical framework built on coupling carrier kinetics with a full-wave time-domain Maxwell equation

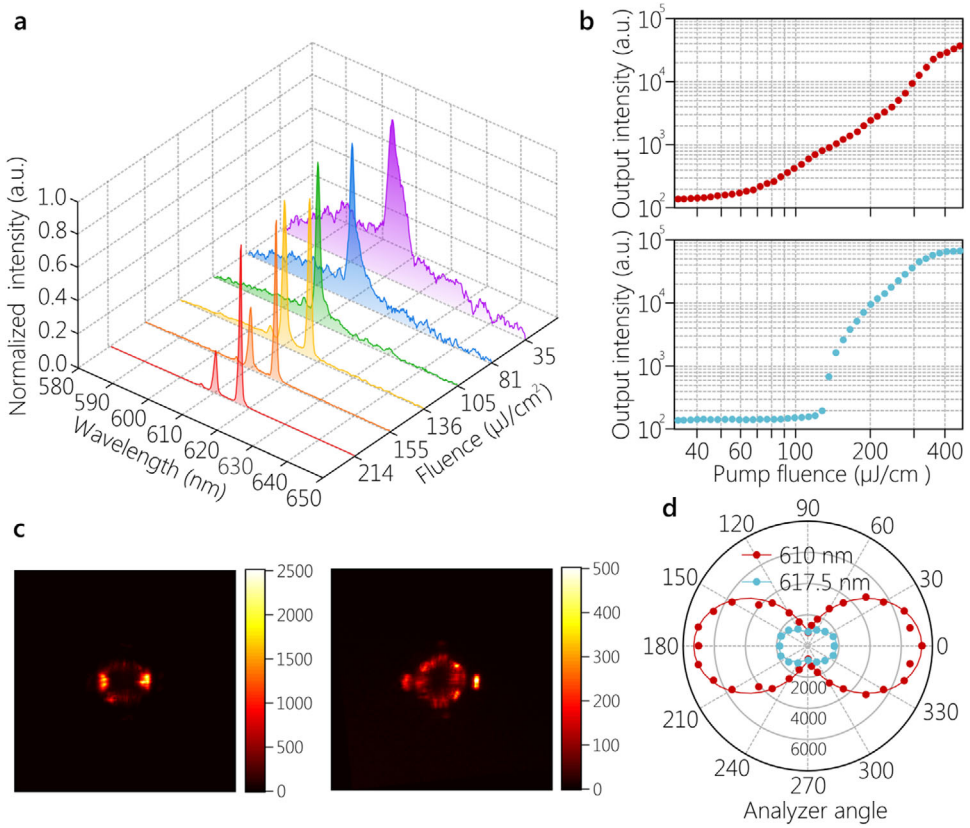

Figure 4. Dual-mode lasing action from dielectric arrays. a) The evolution of the lasing spectrum with pump fluence. b) The output intensity of the lasing peak at 610 nm (top) and 617.5 nm (bottom) as a function of pump fluence. c) Back-focal plane image of the laser emission above the threshold at an analyzer angle of 0° (left) and 90° (right). d) The intensity of the dual laser emission as a function of the polarizing analyzer angle.

solver. Using the developed framework to engineer the electric and magnetic dipole modes in dielectric resonators, we utilize the feedback from the high-Q factor structures to experimentally realize and explore multi-mode lasing. Our results open exciting paths for combining different physical mechanisms in a single dielectric array without intricate resonator designs. We believe that our study could enable advanced, controllable engineering of light–matter interactions with prospective applications to the topological states engineering and quantum light generation.

4. Experimental Section

Metasurface Fabrication: The fabrication process started with creating the required pattern on a silica substrate using a positive-tone resist (ZEP 520A) using electron beam lithography. The silica glass substrates (commercially available optical quality glass from PG&O) were cleaned in solvent (toluene, acetone, IPA) followed by a dehydration bake at 160°C for 2–5 min. At this stage, ZEP 520A electron-beam resist (commercially available from ZEON Chemicals) was spin-coated onto the dry substrate and cured at 180 °C for 3 min. The thickness of the resist should match the desired nanocylinder height. The spin process conditions were varied according to the spin-sheet to arrive at the desired thickness denoted as *h*. Before exposing the resist to electron-beam, a very thin (≈5 nm) layer of Cr metal was deposited onto the resist coated substrate using the e-beam deposition technique to avoid charging related writing discrepancies on a dielectric substrate (Figure S6a, Supporting Information). Following the deposition, the sample was immediately loaded onto the load lock of the electron beam lithography instrument to prevent further oxidation of the Cr thin film. After electron beam exposure, the first Cr layer was etched away using Cr-16 chromium etchant solution and followed by a DI rinse. Next, the resist was developed in ZDMAC developer for 90 s and rinsed in IPA. Some undeveloped residual resist may remain at the bottom of the narrow cylinder holes which were then cleaned off by ashing the resist in a barrel etcher in O_2 plasma (at 100 W, 1.2 T) for 1 min. This may lead to some reduction of the resist thickness from top-down etching as well as an increase in the diameter of the cylinders. Initial resist thickness and written diameter of the cylinders can be adjusted to account for this step. At this point, the sample should have an array of cylindrical holes in the resist (Figure S6b, Supporting Information).

Next, the sample was loaded onto an atomic layer deposition (ALD) tool for the growth of the TiO_2. ALD allowed for uniform and highly conformal layer by layer growth and therefore ensured complete coverage of all the holes (Figure S6c, Supporting Information). The TiO_2 thickness was decided by the maximum diameter of the cylinders (*d*) on the sample. Due to conformal growth from all sides thickness of *d*/2 would be enough to fill the cylinders (Figure S6d, Supporting Information). However, a margin of growing an additional 10–15 nm was kept. In order to ensure the stability of the polymer-based resist, the ALD operating temperature was kept much below the resist curing temperature, in this case, at a 120 °C. A low growth rate of 0.6 nm per cycle was achieved in this low-temperature process. In addition, other process parameters such as precursor and water pulse times, purge times, pressure, etc. were also optimized to arrive at a reasonably good optical quality of the grown TiO_2 film. At this stage, TiO_2 covered not only the cylinder holes but also the top surface of the resist. To planarize the top surface and also to expose the resist layer from the top,

at this step, the excess TiO_2 cover was etched away using a plasma RIE technique. A combination of BCl3, Cl2, and Ar gas chemistry was used at 650 W RF power, 80 W bias power, and 0.8 T pressure (Figure S6e, Supporting Information).

The remaining resist matrix can then be removed in *N*-Methyl Pyrrolidine heated at 120 °C followed by rinsing the sample in acetone and IPA. This concluded the fabrication of the high aspect ratio (Figure S6f, Supporting Information).

Characterization: The fabricated metasurfaces were characterized by measuring the transmittance spectra at normal incidence for both p- and s-polarizations. This took place after the TiO_2 etching but before the removal of resist. The resist polymer had a refractive index of around 1.45 and therefore satisfied the index matching condition with the substrate. Optical characterization was performed using the J.A. Woollam V-VASE UV–vis–NIR variable angle spectroscopic ellipsometer. The measured transmittance spectra at different R_{cyl} of the resonators are given in Figure S4a, Supporting Information with solid lines showing the p-polarization and dashed lines corresponding to the s-polarization of the incident light. It can be clearly observed that under normal illumination, the metasurfaces responses were polarization-independent. Additionally, the simulated transmittance as a function of R_{cyl} and wavelength is shown in Figure S4b, Supporting Information. Dashed lines indicated the radii corresponding to the measurements in Figure S4a, Supporting Information with red, blue, and green indicating $R_{cyl} = 85$ nm, $R_{cyl} = 90$ nm, and $R_{cyl} = 95$ nm, respectively. As evident from Figure S4, Supporting Information, the measured transmittance of different samples was generally in good agreement with the predictions from the simulations. Deviations between experimental and simulated data were believed to be due to the fabrication imperfections as non-uniformity was observed in the radii values of the nanoresonators of the same sample. This led to spectral broadening, causing a reduction in the Q-factors as well as a shift in the location of the resonances.

Lasing Measurements: To study lasing properties with the metasurface feedback, a frequency-doubled Nd: YAG picosecond laser was used. The laser generated pulses with a carrier wavelength of 532 nm, a pulse width of 400 ps, and a repetition rate of 1 Hz. A schematic of the setup is shown in Figure S7, Supporting Information. The laser beam that pumped the metasurface was focused down to 100 µm with a 5× objective. The light emission from the sample was collected with a fiber, which was then fed to a spectrometer equipped with a charge-coupled device (CCD). A notch filter centered around 532 nm was used to block the pump. All lasing measurements were done in air at room temperature. Another CCD was used to image the sample plane for sample selection and alignment and also to ensure an accurate estimation of the pump spot size. Back focal plane measurements were carried out with the same setup as lasing by redirecting the laser emission from the spectrometer to a CCD through a lens that was adjusted to form a back focal plane image at the camera sensor.

Finite Difference Time Domain Simulations of Lasing Dynamics: An in-home built framework of a multi-level system[37–39] incorporated in a commercial software finite difference time domain solver[40] was utilized to model nonlinear light–matter interactions.[41,42] The multi-level framework allowed for capturing the behavior of the gain materials embedded in photonic nanostructures and had an accurate estimate of their threshold and spectral response. In this work, the gain medium (Rhodamine 101) was modeled using a four-level system, and the electromagnetic waves were treated classically with Maxwell's equations.[37] The four-level atomic system used was depicted in Figure S5, Supporting Information. More details can be found in Section S3, Supporting Information.

Supporting Information

Supporting Information is available from the Wiley Online Library or from the author.

Acknowledgements

The authors acknowledge the financial support by the U.S. Department of Energy (DOE), Office of Basic Energy Sciences (BES), Division of Materials Sciences and Engineering under Award DE-SC0017717 (sample fabrication), the U.S. Office of Naval Research under award number N00014-21-1-2026 (optical characterization), and the DARPA/DSO Extreme Optics and Imaging (EXTREME) Program under Award HR00111720032 (theory/numerical modeling).

Conflict of Interest

The authors declare no conflict of interest.

Keywords

bound states in the continuum, dielectric resonances, nanolasers, nonlinear light–matter interactions

Received: September 20, 2020
Revised: November 27, 2020
Published online: January 27, 2021

[1] J. von Neumann, E. Wigner, *Z. Phys.* **1929**, *30*, 465.
[2] J. Lee, B. Zhen, S.-L. Chua, W. Qiu, J. D. Joannopoulos, M. Soljačić, O. Shapira, *Phys. Rev. Lett.* **2012**, *109*, 067401.
[3] Y. Plotnik, O. Peleg, F. Dreisow, M. Heinrich, S. Nolte, A. Szameit, M. Segev, *Phys. Rev. Lett.* **2011**, *107*, 183901.
[4] N. Moiseyev, *Phys. Rev. Lett.* **2009**, *102*, 167404.
[5] H. Friedrich, D. Wintgen, *Phys. Rev. A* **1985**, *32*, 3231.
[6] C. W. Hsu, B. Zhen, A. D. Stone, J. D. Joannopoulos, M. Soljačić, *Nat. Rev. Mater.* **2016**, *1*, 16048.
[7] H. M. Doeleman, F. Monticone, W. den Hollander, A. Alù, A. F. Koenderink, *Nat. Photonics* **2018**, *12*, 397.
[8] C. W. Hsu, B. Zhen, J. Lee, S.-L. Chua, S. G. Johnson, J. D. Joannopoulos, M. Soljačić, *Nature* **2013**, *499*, 188.
[9] Z. F. Sadrieva, I. S. Sinev, K. L. Koshelev, A. Samusev, I. V. Iorsh, O. Takayama, R. Malureanu, A. A. Bogdanov, A. V. Lavrinenko, *ACS Photonics* **2017**, *4*, 723.
[10] S. I. Azzam, V. M. Shalaev, A. Boltasseva, A. V. Kildishev, *Phys. Rev. Lett.* **2018**, *121*, 253901.
[11] L. Fonda, *Ann. Phys.* **1961**, *12*, 476.
[12] L. Fonda, *Ann. Phys.* **1963**, *22*, 123.
[13] D. C. Marinica, A. G. Borisov, S. V. Shabanov, *Phys. Rev. Lett.* **2008**, *100*, 183902.
[14] M. V. Rybin, K. L. Koshelev, Z. F. Sadrieva, K. B. Samusev, A. A. Bogdanov, M. F. Limonov, Y. S. Kivshar, *Phys. Rev. Lett.* **2017**, *119*, 243901.
[15] A. Krasnok, A. Alú, *J. Opt.* **2018**, *20*, 064002.
[16] E. N. Bulgakov, A. F. Sadreev, *Phy. Rev. B* **2008**, *78*, 075105.
[17] Z. Yu, X. Xi, J. Ma, H. K. Tsang, C.-L. Zou, X. Sun, *Optica* **2019**, *6*, 1342.
[18] K. Koshelev, S. Kruk, E. Melik-Gaykazyan, J.-H. Choi, A. Bogdanov, H.-G. Park, Y. Kivshar, *Science* **2020**, *367*, 288.
[19] A. Leitis, A. Tittl, M. Liu, B. H. Lee, M. B. Gu, Y. S. Kivshar, H. Altug, *Sci. Adv.* **2019**, *5*, eaaw2871.
[20] A. Kodigala, T. Lepetit, Q. Gu, B. Bahari, Y. Fainman, B. Kanté, *Nature* **2017**, *541*, 196.
[21] S. T. Ha, Y. H. Fu, N. K. Emani, Z. Pan, R. M. Bakker, R. Paniagua-Domínguez, A. I. Kuznetsov, *Nat. Nanotechnol.* **2018**, 1.
[22] C. Huang, C. Zhang, S. Xiao, Y. Wang, Y. Fan, Y. Liu, N. Zhang, G. Qu, H. Ji, J. Han, L. Ge, Y. Kivshar, Q. Song, *Science* **2020**, *367*, 1018.
[23] K.-Y. Jeong, M.-S. Hwang, J. Kim, J.-S. Park, J. M. Lee, H.-G. Park, *Adv. Mater.* **2020**, 2001996.
[24] V. Mylnikov, S. T. Ha, Z. Pan, V. Valuckas, R. Paniagua-Dominguez, H. V. Demir, A. I. Kuznetsov, *ACS Nano* **2020**, *14*, 7338.
[25] E. Tiguntseva, K. Koshelev, A. Furasova, P. Tonkaev, V. Mikhailovskii, E. V. Ushakova, D. G. Baranov, T. Shegai, A. A. Zakhidov, Y. Kivshar, S. V. Makarov, *ACS Nano* **2020**, *14*, 8149.

[26] M. Wu, S. T. Ha, S. Shendre, E. G. Durmusoglu, W.-K. Koh, D. R. Abujetas, J. A. Sánchez-Gil, R. Paniagua-Dominguez, H. V. Demir, A. I. Kuznetsov, *Nano Lett.* **2020**, *20*, 6005.
[27] A. I. Kuznetsov, A. E. Miroshnichenko, M. L. Brongersma, Y. S. Kivshar, B. Luk'yanchuk, *Science* **2016**, *354*, aag2472.
[28] M. F. Limonov, M. V. Rybin, A. N. Poddubny, Y. S. Kivshar, *Nat. Photonics* **2017**, *11*, 543.
[29] J. Van de Groep, A. Polman, *Opt. Express* **2013**, *21*, 26285.
[30] A. B. Evlyukhin, C. Reinhardt, B. N. Chichkov, *Phys. Rev. B* **2011**, *84*, 235429.
[31] V. E. Babicheva, J. V. Moloney, *Nanophotonics* **2018**, *7*, 1663.
[32] J. Li, N. Verellen, P. Van Dorpe, *J. Appl. Phys.* **2018**, *123*, 083101.
[33] V. E. Babicheva, A. B. Evlyukhin, *Laser Photonics Rev.* **2017**, *11*, 1700132.
[34] Y. Yang, I. I. Kravchenko, D. P. Briggs, J. Valentine, *Nat. Commun.* **2014**, *5*, 5753.
[35] S. Campione, S. Liu, L. I. Basilio, L. K. Warne, W. L. Langston, T. S. Luk, J. R. Wendt, J. L. Reno, G. A. Keeler, I. Brener, M. B. Sinclair, *Acs Photonics* **2016**, *3*, 2362.
[36] D. Wang, A. Yang, W. Wang, Y. Hua, R. D. Schaller, G. C. Schatz, T. W. Odom, *Nat. Nanotechnol.* **2017**, *12*, 889.
[37] S. I. Azzam, J. Fang, J. Liu, Z. Wang, N. Arnold, T. A. Klar, L. J. Prokopeva, X. Meng, V. M. Shalaev, A. V. Kildishev, *Laser Photonics Rev.* **2019**, *13*, 1800071.
[38] S. I. Azzam, A. V. Kildishev, *Opt. Mater. Express* **2018**, *8*, 3829.
[39] S. I. Azzam, A. V. Kildishev, *Nanophotonics* **2018**, *8*, 145.
[40] Lumerical, http://www.lumerical.com/tcad-products/fdtd (accessed: November 2020).
[41] K. Yee, *IEEE Trans. Antennas Propag.* **1966**, *14*, 302.
[42] S. Chang, A. Taflove, *Opt. Express* **2004**, *12*, 3827.